ELSEVIER

Journal of Nuclear Materials 264 (1999) 295–308

journal of nuclear materials

Study of B_4C microstructure evolution under neutron irradiation by X-ray diffraction profiles analysis

D. Simeone *, D. Gosset, D. Quirion, X. Deschanels

Commissariat à l'Energie Atomique, Ctr. d'Etudes de Saclay, Laboratoire d'Etude des Matériaux Absorbants, F-91191 Gif sur Yvette cedex, France

Received 14 May 1998; accepted 27 July 1998

Abstract

During neutron irradiation of boron carbide, helium bubbles nucleate, inducing cracks and then reducing lifetime of control rods. The role of helium bubbles has been clearly identified by Transmission Electron Microscopy (TEM) photographs. X-ray diffraction may be a complement to TEM studies of B_4C microstructure evolution under irradiation. In this article, we show that X-ray profiles may be used to calculate a mean bubble density and a local strain value as a function of neutron irradiation. Both the data are useful to present a quantitative analysis of the mechanism responsible for the damage of irradiated B_4C material. To observe an eventual solubility of helium atoms in the B_4C matrix, we have performed different isochronal annealing on irradiated B_4C samples. Results of X-ray diffraction experiments on both irradiated and annealed samples permit to confirm previous works on B_4C behaviour under neutron irradiation and to present a quantitative analysis of irradiated B_4C samples. The study of strain η and Coherent Diffracting Domains (CDD) as a function of $N(\alpha)$, number of neutronic capture per unit volume, exhibits a saturation of η near 1% and a constant increase of CDD up to 4×10^{16} CDD/cm^3. This η and CDD evolution can be explained by helium bubble growth up to a 'characteristic' size in the material during irradiation. Moreover, no second phase has been observed during both irradiation and annealing of B_4C irradiated samples.

1. Introduction

An important part of the control rods used for control and shut down of nuclear reactors are made of boron carbide (B_4C). Because of its low neutron induced radioactivity, low cost and high melting point, B_4C is an attractive material used both in Fast Breeder Reactors (FBR) and in Pressurised Water Reactors (PWR).

During neutron irradiation, $^{10}B(n,\alpha)^7Li$ reaction induces helium formation in the material. After a short irradiation time, helium atoms agglomerate in flat bubbles which induce a large swelling and high stresses, and lead to the destruction of the material [1–3]. Many authors have observed helium bubbles by Transmission Electron Microscopy (TEM) [2–6]. These studies lead to contradictory results as regard to some aspects as nucleation and growth of helium bubbles. Hollenberg [4] claimed that the density and the size of helium bubbles depend on the irradiation temperature whereas Stoto [2] mentioned that bubbles evolution is controlled only by helium rate production. So, some aspects of B_4C destruction are not quite understood: trapping efficiency and nucleation rate of the bubbles, low helium release rate [3], evolution of internal strain.

The knowledge of strain field evolution in irradiated B_4C samples may be helpful to describe the helium bubbles evolution under irradiation. Moreover, information on the helium atoms diffusion process as a function of the temperature could be obtained by annealing samples. In this frame, X-ray diffraction analysis (study of Bragg angles, line broadening, intensity variations) can be a useful tool to study the microstructure of boron carbide during neutron irradiation.

* Corresponding author. Tel.: +33-1 69 08 29 20; fax: +33-1 69 08 90 82; e-mail: lema@sentl.amts.cea.fr.

0022-3115/99/$ – see front matter
PII: S0022-3115(98)00485-1

In this paper, we present an analysis of X-ray diffraction profile corrections on a Curved Position Sensitive Detector (CPSD) [9–11]. We show that, in our case, the major correction is due to the transparency effect. Then, this correction is applied first to samples irradiated at different $N(\alpha)$ values ($N(\alpha)$ is the number of helium atoms per volume unit produced by the neutron irradiation) and secondly, after successive isochronal annealings. At last, we present an interpretation of line broadening in terms of Coherent Diffracting Domains (CDD) and internal strains. Such an analysis permits us to present a possible degradation mechanism of B_4C under neutron irradiation.

2. Analysis of X-ray diffraction profile errors on a CPSD

Usually, X-ray diffraction analysis of boron carbide is performed on powders with a Bragg Brentano diffractometer [7,8]. To avoid destructive handling B_4C irradiated samples, we analyse bulk samples. Moreover, irradiated B_4C samples are small (platelets of $A = 0.3$ cm radius and 0.2 cm thickness) and composed of low Z elements. We used a CPSD in a Debye Scherrer geometry to obtain accurate X-ray diffraction profiles in half a day, against five days with a classical Bragg Brentano diffractometer. Finally, such a diffractometer allows to study the kinetic evolution of helium bubbles as a function of temperature. But, analysing low Z materials in this geometry leads to high line broadenings and shifts, which need to be carefully corrected before studying intrinsic broadening and cell parameter evolutions.

2.1. Errors associated with the CPSD and Debye Scherrer geometry

Using a CPSD and a Debye Scherrer geometry lead to 4 major systematic errors arising [10] from:

- nonlinearity of CPSD;
- sample displacement;
- beam axial divergence; and
- sample transparency.

Because of its electronics and the structure of the delay line, a CPSD cannot have a linear response between acquisition channels and angular positions. This kind of error has been extensively studied. To correct such an error, we have to perform a linearisation with a well-chosen standard material [10].

The sample displacement error is induced by the displacement of the sample surface by an amount s in the direction perpendicular to the sample surface. It causes a displacement of the diffraction maxima but no broadening effects. The sample displacement error correction in the case of the asymmetric Debye Scherrer geometry is given by the classical formula [12]

$$\Delta 2\theta_s = 2\theta - 2\theta_{th} = \frac{-180 \sin(2\theta_{th})}{\pi R \sin \varphi} s, \quad (1)$$

where R is the detector sample radius (25 cm), s the vertical displacement of the sample, φ the angle between the incident X-ray beam and the flat surface of the sample and $2\theta_{th}$ the angle associated to a null value of s.

The axial divergence is associated to the Debye Scherrer geometry. This effect displaces the lines of the profile and broadens them [12]. For our installation (convergent beam), the focal point is on the CPSD (Fig. 1) and it is possible to determine the centroid displacement associated to the axial divergence. It can be written [13] as follows

$$\Delta 2\theta_{dv} = \frac{t}{2d} \sin(\theta - \varphi) \cos(\theta), \quad (2)$$

where t (0.02 cm) is the slit size (5 cm ahead the sample) and d the monochromator focal length (53 cm). This error is negligible compared to the transparency error (shift caused by the axial divergence effect on the centroid about 10^{-2} degree and shift associated to the transparency effect about 0.2°).

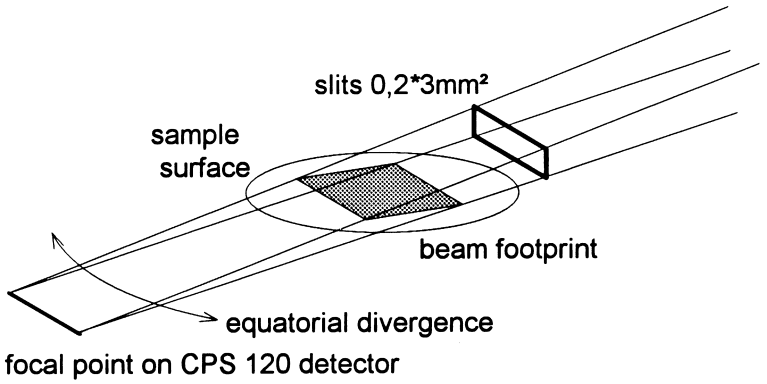

Fig. 1. Position of the focal point, X-ray beam and diverging slit in our experimental Debye Scherrer geometry.

Because the footprint of the X-ray beam is entirely in the sample, the equatorial divergence of the X-ray beam is neglected.

2.2. Transparency error in Debye Scherrer geometry

The transparency effect deforms asymetrically the diffraction line profile and contributes to the displacement of the maximum angle of diffraction (Fig. 2). This effect is due to the diffraction of X-rays not only at the surface of the sample but also within its body. It is usual to express the recorded diffraction line profile f by a convolution of the diffracted X-ray beam angular distribution g by the intensity distribution associated with the transparency effect h [14].

$$f = h * g. \tag{3}$$

Let us consider an ideal elementary X-ray beam penetrating into a flat specimen with an absorption coefficient μ (cm^{-1}) at an incident angle φ. At a point P inside the sample, we can calculate the total path length of a photon that penetrates the sample at O and is diffracted at P.

$$\mathrm{OP} = \frac{y}{\sin(\varphi)}, \qquad \mathrm{PM} = \frac{y}{\sin(2\theta - \varphi)}. \tag{4}$$

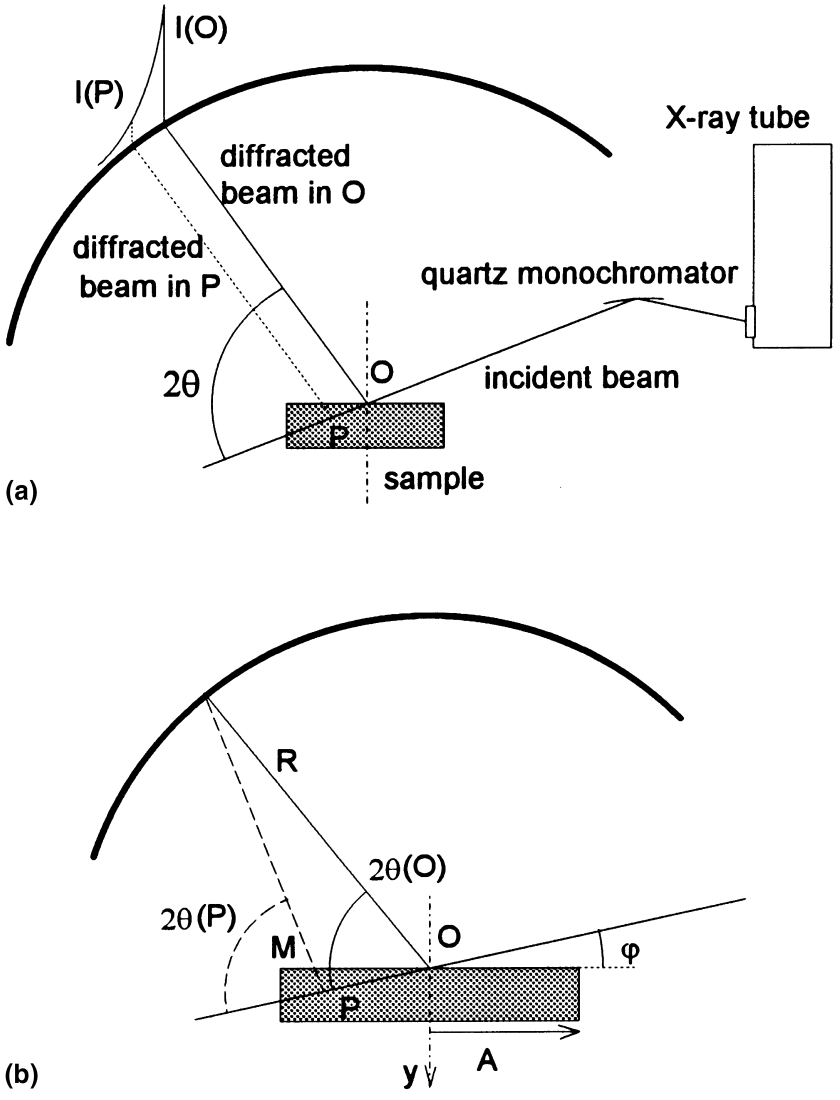

Fig. 2. (a) Presentation of the diffracted profile modified by transparency effect. $I(O)$ diffracted intensity from the point O collected on the CPSD at the angle $2\theta(0)$, $I(P)$ diffracted intensity from the point P collected on the CPSD at the angle $2\theta(0)$. The transparency effect induces a diffracted intensity profile. (b) Notations used in this paper.

Then the part of the X-ray beam diffracted at the point P is reduced in intensity by a factor: $\exp(-a(2\theta(P))y)$, where

$$a(2\theta(P)) = \mu\left(\frac{1}{\sin\ \varphi} + \frac{1}{\sin(2\theta(P) - \varphi)}\right). \tag{5}$$

Some of the diffracted beams emerge from the side of the sample. The contributions of such X-rays to the diffracted profiles are less than 10% for the irradiated B_4C samples and only affect the foot of low angle X-ray diffracted profiles. Therefore, they are ignored in our analysis. Moreover, our calculations were done by considering that the analysed depth is always smaller than the sample thickness. This condition is written as

$$A\ \tan\varphi < e. \tag{6}$$

This condition is always satisfied in the experiments ($A = 0.3$ cm, $e = 0.2$ cm and φ is equal to 10°).

Then the intensity distribution associated to the transparency effect can be written as

$$h_t = \begin{cases} \exp(-a(2\theta)y) & 0 < y < A\ \tan\varphi, \\ 0 & \text{else.} \end{cases} \tag{7}$$

It is now possible to obtain the profile f when g is supposed to be gaussian taking into account the transparency effect.

$$f_g(x) = \int_0^\infty h_t(y) \exp\left(\frac{-(x-uy)^2}{2\Delta^2}\right) \frac{dy}{\Delta\ \sin\varphi\sqrt{2\pi}}, \tag{8}$$

where $x = 2\theta(P) - 2\theta_0$, $u = \sin 2\theta(P)/R\sin\varphi$ (displacement error associated to the point P) and θ_0 is the Bragg angle associated to the considered peak and Δ the width of the gaussian function.

A similar calculation for a Lorentzian line shape leads to

$$f_L(x) = \int_0^\infty h_t(y)(b + (x-uy)^2)^{-1}\ dy, \tag{9}$$

where b is the width of the Lorentzian function.

It is now possible to calculate all profiles using a pseudo-Voigt function. To carry on our calculation, we assume that the maximum X-ray diffraction angle at the point P can be replaced in the exponential term (Eq. (5)) by the X-ray diffraction peak at the point O. Then $a(2\theta(P)) \cong a(2\theta(0)) \cong a$. It becomes now possible to obtain explicitly the profile $f(x)$ (see Appendix A). Fig. 3(a) and (b) present comparisons between calculated and collected diffraction lines for low (37.5°) and large angles (122.5°) for non-irradiated B_4C samples.

We observed that experimental and calculated profiles, obtained using gaussian profiles for both irradiated and non-irradiated B_4C samples, are always closed to each other in our study. Consequently, a gaussian profile is sufficient to simulate $g(x)$. In this case, we can write the $f(x)$ profile taking into account the transparency effect

$$f(\xi) = \exp(-2D(\xi - D)) \times \frac{\mathrm{Erf}(BA\ \tan\varphi + 2D + \xi) - \mathrm{Erf}(\xi)}{\mathrm{Erf}(BA\ \tan\varphi + 2D + \xi) - \mathrm{Erf}(D)}, \tag{10}$$

with

$$D = \frac{\mu\Delta R}{\sin 2\theta_m\sqrt{2}}\left(1 + \frac{\sin\varphi}{\sin(2\theta_m - \varphi)}\right),$$

$$\xi = D + \frac{(2\theta - 2\theta_0)}{\Delta\sqrt{2}},$$

$$B = \frac{\sin 2\theta_m}{R\sin\varphi\,\Delta\sqrt{2}}.$$

In our experimental conditions, $R = 25$ cm, $A = 0.3$ cm, $\mu = 5.5$ cm^{-1}, $\Delta > 0.05°$ and $\varphi = 10°$. Thus, $AB\ \tan\varphi$ is larger than 100. The function f can be simplified as

$$f(\xi) = \exp(-2D(\xi - D))\frac{1 - \mathrm{Erf}(\xi)}{1 - \mathrm{Erf}(D)}. \tag{11}$$

This function $f(\xi)$ permits to define totally the gaussian function $g_{\theta,\Delta}(\xi)$ which gives much information on the material microstructure.

2.3. Study of $g(x)$ profile lines

We now focus our attention on the $g(\xi)$ function. We apply the model of integral breadth to describe the microstructure evolution in terms of strain field and size effect associated with broadening of B_4C profiles [11,13]. Our main hypothesis is that size and strain broadening of X-ray diffraction peaks are independent and can be added. We note b the integral breadth defined by

$$b = \frac{\int_{-\infty}^{\infty} g(2\varepsilon)\,d2\varepsilon}{g(0)}, \tag{12}$$

where $g(0)$ is the maximum of the $g(\xi)$ function.

The intrinsic profiles $g(2\varepsilon)$ are assumed to be gaussian. Then, it is possible to study strain and size effects using a gaussian decomposition.

Denoting $s = 2\ \sin\theta/\lambda$ the diffraction vector, the integral breadth is linked to s by the following formula.

$$\Delta b^2\frac{\cos^2\theta}{\lambda^2} = (b^{*2} - b^2)\frac{\cos^2\theta}{\lambda^2} = \left(\frac{k}{L}\right)^2 + (2\eta)^2 s^2, \tag{13}$$

where (L/k) is the apparent size of CDD, k the Scherrer constant depending on the (hkl) line and varying from 1 to 1.6 [15] and η an evaluation of the maximum strain inside the material. The star refers to the irradiated material. To estimate irradiation effects, we subtract all intrinsic effects associated to the non-irradiated material (finite size grain, stacking faults, twins). Moreover, such a substraction permits to take into account minor aberrations like spectral dispersion, equatorial diver-

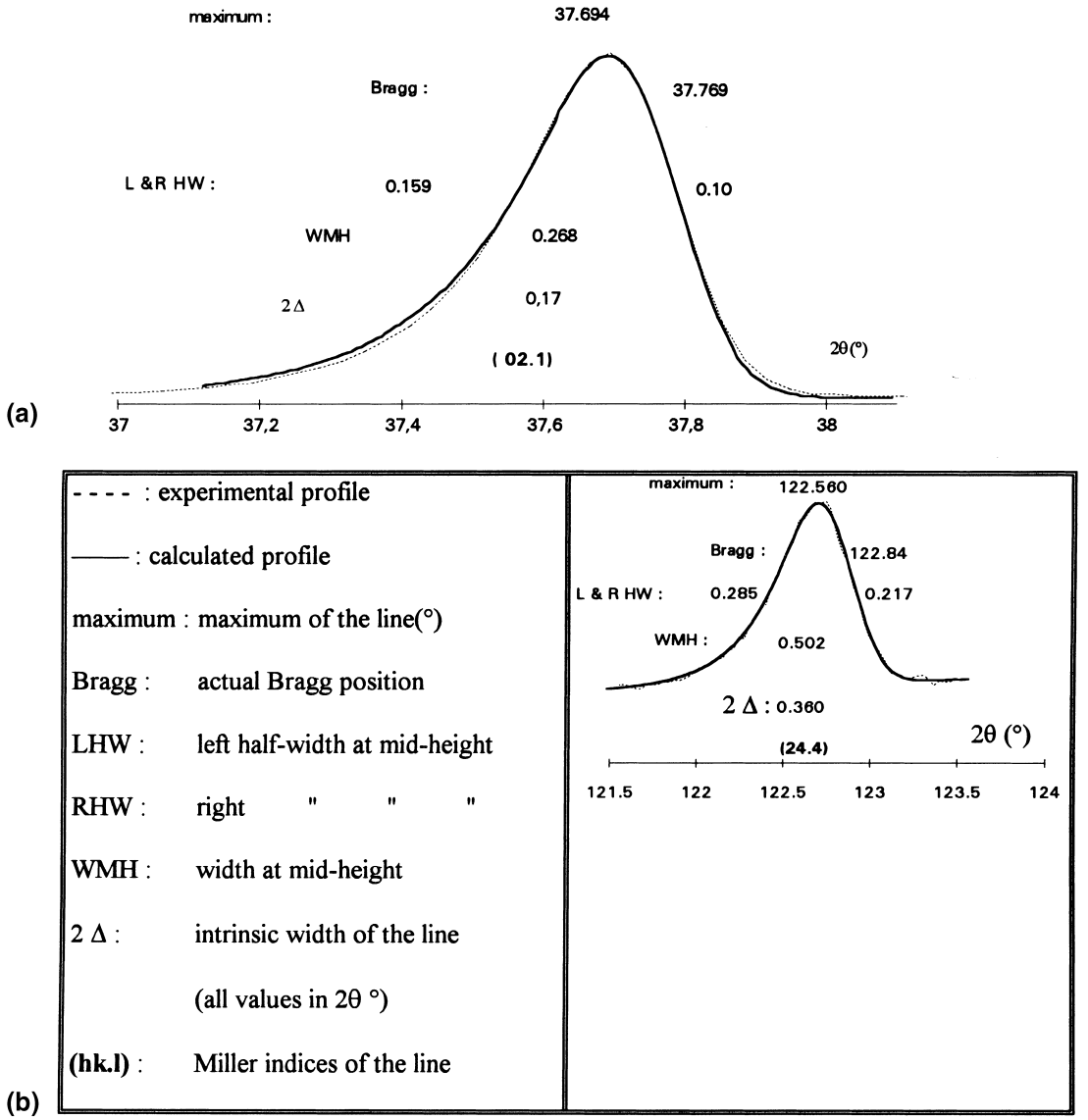

Fig. 3. (a) Comparison between simulated profile obtain for a gaussian $g(2\varepsilon)$ profile and experimental profile for low diffraction angles. (b) Comparison between simulated profile obtain for a gaussian $g(2\varepsilon)$ profile and experimental profile for large diffraction angles.

gency and detector aberration, which are all supposed to be gaussian. In fact, collected $b(2\theta)$ can be written as

$$b^2(2\theta) = b_s^2(2\theta) + b_e^2(2\theta) + b_d^2(2\theta) + b_i^2(2\theta),$$

where $b_s(2\theta)$ is the integral breadth due to incident beam size aberration, $b_e(2\theta)$ the breadth due to equatorial divergency of the X-ray beam, $b_d(2\theta)$ the breadth due to detector aberration and $b_i(2\theta)$ the intrinsic breadth associated to $g(2\theta)$. These aberrations are similar for irradiated and non-irradiated samples. Then, using a non-irradiated sample permits to correct these aberrations [11,16,17].

A reasonable interpretation of CDD is that microstructure evolution of the material under irradiation subdivide the original crystallites (grains) into much smaller CDDs. These domains are sufficiently disoriented to scatter incoherently. Thus, they can be understood as small 'virtual' crystallites. The strain associated to this CDD is an approximate upper limit of the lattice distorsion [13].

X-ray diffraction peak measurements permit us to obtain mean CDD size and strain in irradiated samples. To study the anisotropy of these values, we have analysed the X-ray diffraction peaks associated to the $\langle 1\ 1\ 1 \rangle$

directions and [1 1 1] planes. Comparisons between CDD size, strains and cell parameters after irradiation and isochronal annealings will allow us to have a detailed description of the B_4C behaviour under neutron irradiation.

3. Experimental details

3.1. Diffractometer configuration

All experiments carried out for this study were performed on a diffractometer equipped with a vertical INEL CPS 120 detector in the Debye Scherrer geometry with the following conditions.

- Incident beam comes from a copper sealed X-ray tube (generator power set at 30 mA × 40 kV) through a bent quartz monochromator selecting the CuKα1 radiation ($\lambda = 1.540598$ Å).
- Thin slits (5 cm ahead the sample) limit the beam to a 1.2×3 mm^2 section on the sample.

To linearise the CPSD, we use Y_2O_3 (space group Ia3, $a = 10.603$ Å) which possesses 67 reflection peaks uniformly distributed in the angular range between 20 and 140°. Fig. 4 presents experimental FWMH^2 of Y_2O_3 as a function of tan(θ). These data are well described by a Cagliotti function.

3.2. Samples preparation

Irradiated and non-irradiated B_4C samples were obtained by hot pressing of B_4C powders. Analysed B_4C pellets had an initial boron isotopic composition $N(^{10}B)/N(B)$ close to 48%, where $N(X)$ is the number of the chemical elements X per cm^3. The grain size of samples before irradiation was about 10 μm and the porosity of samples about 3%. Polycrystalline B_4C pellets were irradiated 399 days (FBR Phenix french reactor) in a stainless steel clad. Porous plugs at both ends of the cladding allow cooling of the pellets by a constant liquid sodium flux. The objective of such type of reactors is to avoid the self-shielding of ^{10}B with thermal neutrons (25 MeV) and thus to obtain ^7Li and ^4He production profiles uniform along the radius of the pellets. Final neutron captures per unit volume $N(\alpha)$, calculated from boron isotopic ratio determination, vary from 12×10^{20} to 96×10^{20} captures/cm^3. No thermocouples were used to measure the irradiation temperature of B_4C pellet. We have estimated the temperature of each sample solving the steady state heat equation with a heat production rate due to the $^{10}B(n,\alpha)^7Li$ reaction constant equal to $N(\alpha)/t_{irr}(t_{irr} = 399$ days) and a thermal conductivity of irradiated boron carbide of 5.7 W m^{-1} K^{-1} [19]. To obtain clean B_4C samples, fragments with about 1 cm initial size have been cut with a diamond wire saw into

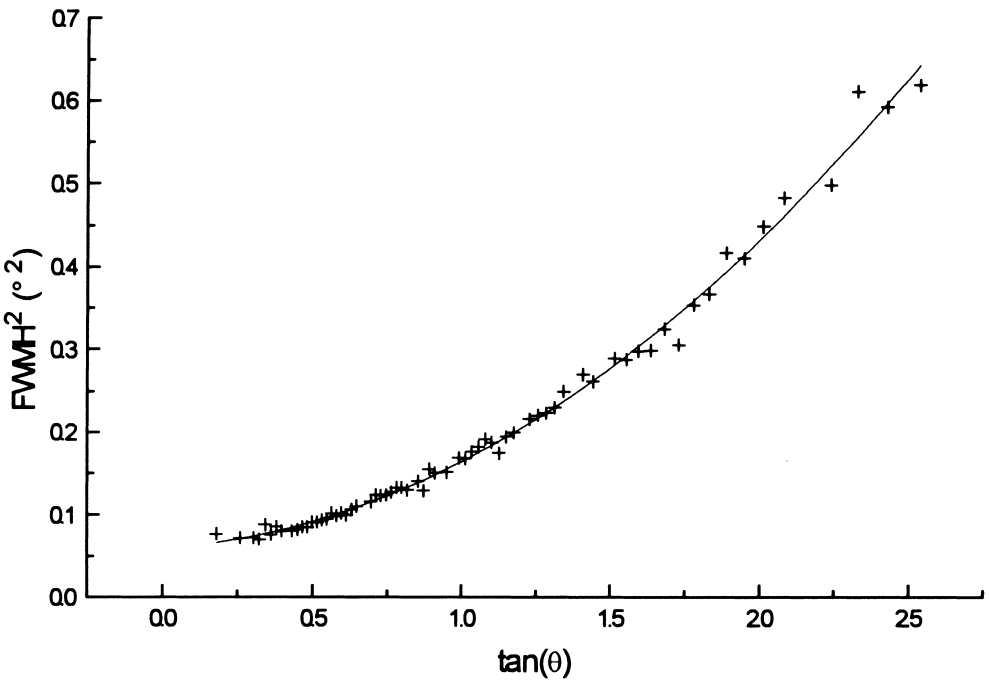

Fig. 4. Graph of the FWMH of Y_2O_3 as a function of X-ray diffracted angles 2θ. The Cagliotti associated function can be written as $0.06 + 0.023 \tan(\theta) + 0.081 \tan^2(\theta)$.

0.2 cm thickness flat slabs. Only fresh B_4C surfaces were then analysed by the X-ray diffraction.

3.3. Isochronal annealing of B_4C samples

We have annealed at increasing temperatures, from 800°C to 2200°C by steps of 200°C, a 12×10^{20}captures/cm^3 irradiated B_4C sample. The aim of this study is to show a possible growth of helium bubbles and stress relaxation around bubbles as a function of annealing temperature. In fact, the growth of helium bubbles in irradiated B_4C should induce a diminution of the internal strain field in the material and then a diminution of the broadening of all X-ray diffraction peaks. To avoid migration of helium out of the pellet, we need to minimise the annealing time. Using diffusion coefficient of helium in boron carbide [20], we have calculated the maximum quantity of helium able to migrate outside of the pellet during the annealing using the unidimensional diffusion equation formula.

$$\frac{Q(t)}{Q_0} = \sum_{p=0}^{\infty} \frac{8}{(2p+1)^2\pi^2} \exp\left(- (2p+1)^2 \frac{Dt}{4e^2} \right), \qquad (14)$$

where Q_0 is the initial quantity of helium present before the annealing in the sample, D the helium diffusion coefficient, t the annealing time and e the thickness of the sample. To allow growth of bubbles, helium atoms need to have enough time to be trapped by a bubble in a diffusion process. The characteristic time for a diffusion process is roughly equal to

$$\tau = \frac{l^2}{D}, \qquad (15)$$

where l is the mean length between two bubbles. This mean length was supposed to be equal to typical CDD size (see Section 5.1). The annealing time is then a compromise between these two times. We have chosen from these criteria an annealing time of 30 min. Table 1 presents the ratio of helium release as a function of annealing temperature and Table 2 presents the characteristic time associated to the diffusion process for different temperatures. We can see that the major part of helium atoms remain in the material. Above 800°C, the chosen annealing time (30 min) is much greater than the characteristic time for helium atoms to go inside existing helium bubbles. Then modifications of the helium bubble size can be detected by analysing X-ray diffraction profiles.

3.4. Cell parameter analysis

A classical way to obtain accurate cell parameters is to use the well-known Rietveld method [21,22]. But for our irradiated B_4C samples, it is quite difficult to define a correct ab initio structure because no correct model of B_4C behaviour under irradiation exists nowadays. To obtain cell parameters as a function of both $N(\alpha)$ and temperatures values, we use an unit weight least square method developed by Cohen [23] taking always the same set of 6 well-defined X-ray diffraction peaks (such peaks are not convoluted even for the more irradiated B_4C sample associated to a $N(\alpha)$ value of 96×10^{20} captures/cm^3, see Table 3). Cohen's method was first tested on an NBS silicium sample and lead to the cell parameter value given by international tables (5.43094 Å), taking into account error bars. Consequently, it is possible to deduce an evolution of B_4C cell parameters quite accurately.

4. Results

4.1. Structure of boron carbide

Non-irradiated B_4C possesses a rhombohedral unit cell and belongs to the D^5_{3d} R-3m space group. The structure is composed of icosahedra clusters on the vertex of the rhombohedra linked together by covalent bond and a CBC linear chain in the $\langle 1\ 1\ 1 \rangle$ direction (rhombohedral notation) [18]. The unit cell composition is $(B_{11}C)CBC$ for the standart B_4C samples we used. During irradiation, $^{10}B(n,\alpha)^7Li$ reaction leads to the formation of helium and lithium atoms in the lattice. TEM photographs show the presence of anisotropic

Table 1
Evolution of the helium concentration retained in irradiated B_4C for different annealing temperatures with an annealing time of 30 min

Temperature (°C)	$D^*_{he}t/4e^2$	$Q(t)_{he}/Q_0$	$D^*_{li}t/4e^2$	Q_{li}/Q_0
600	1.06×10^{-12}	0.901	1.04×10^{-11}	0.901
800	2.85×10^{-11}	0.901	9.19×10^{-11}	0.901
1000	2.72×10^{-10}	0.901	4.09×10^{-10}	0.901
1200	1.41×10^{-09}	0.901	1.22×10^{-09}	0.901
1400	4.92×10^{-09}	0.901	2.78×10^{-09}	0.901
1600	1.32×10^{-08}	0.901	5.33×10^{-09}	0.901
1800	2.91×10^{-08}	0.901	9.02×10^{-09}	0.901
2000	5.60×10^{-08}	0.901	1.39×10^{-08}	0.901
2200	9.70×10^{-08}	0.901	2.00×10^{-08}	0.901

Table 2
Evolution of diffusion characteristic time as a function of temperature in B_4C

Temperature (°C)	$\tau = 1/4D_{he}$ (s)
600	3900
800	145
1000	15.2
1200	2.9
1400	0.84
1600	0.31
1800	0.14
2000	0.07
2200	0.04

Table 3
Set of X-ray diffraction peaks used for cell parameters determination

Reference sample peak position (in degrees)	*hkl*
34.991	104
37.835	021
50.322	211
53.520	205
61.815	303
95.176	324

helium bubbles in the [1 1 1] planes and an heavy anisotropic stress field around them.

Rhombohedral length and angle vary respectively from 5.167 to 5.225 Å and from 65.3° to 66.3°. TEM photographs have shown that helium bubbles nucleate in [1 1 1] planes (rhombohedral notation) during neutron irradiation. The anisotropy of bubbles shape induces a strongly anisotropic strain field of main component along ⟨1 1 1⟩ direction. From X-ray diffraction peak analysis, the same anisotropic form of strains is expected. We have then studied in details two distinct peak families. The selection of these families was made calculating the interplanar angle ϕ between a (*hkl*) and the (1 1 1) planes. Peaks with low values ϕ are associated to the [1 1 1] planes and peaks with high values of ϕ to the ⟨1 1 1⟩ direction.

4.2. Line broadening versus $N(\alpha)$

Fig. 5 shows Δb^2 versus s^2 for a specimen irradiated at 48.6×10^{20} captures/cm^3, for ⟨1 1 1⟩ (Fig. 5(a)) direction and [1 1 1] planes (Fig. 5(b)). Corresponding linear regressions are also plotted. A good correlation between Δb^2 and s^2 is obtained (linear coefficient of determination above 0.94). We can then deduce (Figs. 6 and 7) the evolution of CDD concentration (calculated as $k_p^2 k_c / L_p^2 L_c$) and strain for different $N(\alpha)$ values. Tables 4 and 5 summarise these results. A systematic increase of CDD is observed. Fig. 7 shows first an increase and then a saturation of strain value in both ⟨1 1 1⟩ direction and [1 1 1] planes. It also shows an anisotropic distribution of strain in the [1 1 1] planes and in the ⟨1 1 1⟩ direction in agreement with TEM observations [4].

4.3. Line broadening versus annealing temperature

The less irradiated sample has also been submitted to the lowest irradiation temperature. So, the nucleation and the growth of helium bubbles are less advanced. The probability to find helium atoms in solid solution after the neutron irradiation is then the most important in this sample. Such a sample has been annealed to study an eventual microstructure evolution.

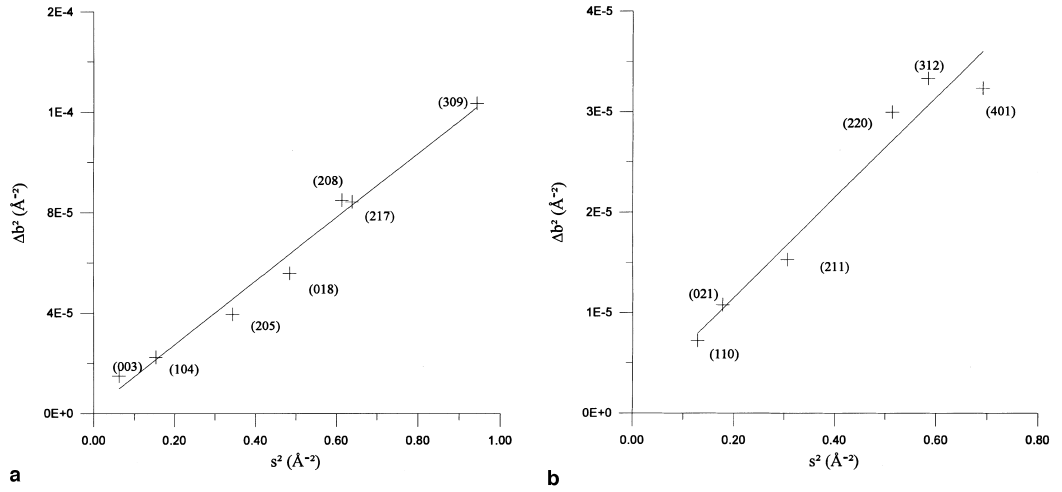

Fig. 5. Δb^2–s^2 curve on irradiated B_4C for $N(\alpha)$ equal to 49×10^{20} captures/cm^3. (a) The Δb^2–s^2 curve in the ⟨1 1 1⟩ direction. (b) The Δb^2–s^2 curve in the [1 1 1] plane. Legend: diffracted peak (*hkl*) associated to each point are given in hexagonal notation.

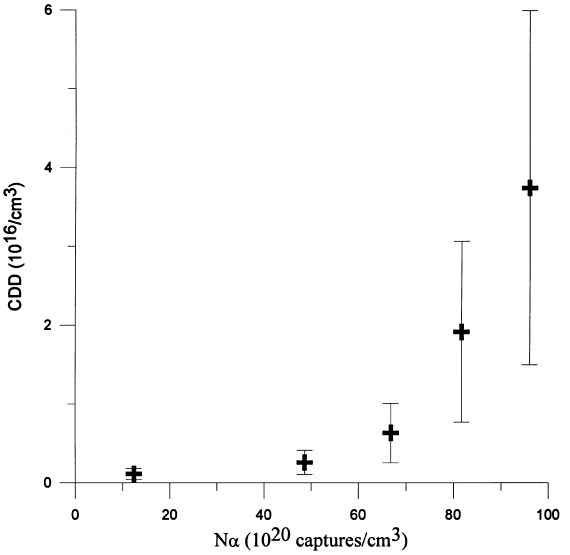

Fig. 6. Evolution of CDD as function of $N(\alpha)$.

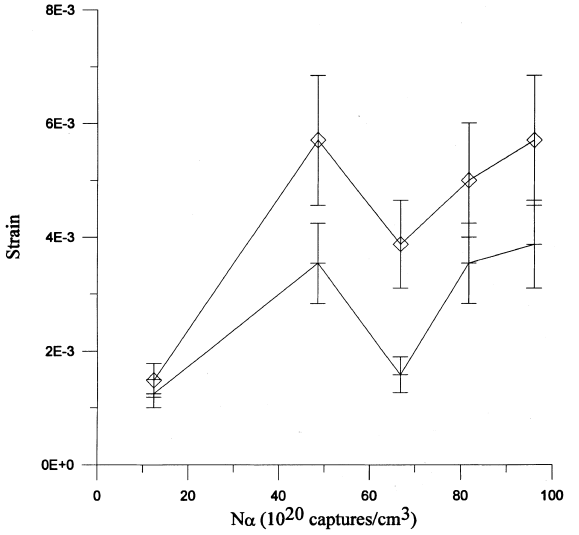

Fig. 7. Evolution of η in $\langle 1\ 1\ 1\rangle$ direction and [1 1 1] planes as function of $N(\alpha)$.

We have examined the evolution of strain and CDD concentration for different annealing temperatures for this sample. Fig. 8 shows no significant evolution for strain up to 1600°C. In the same way, CDD concentrations were constant in the range of studied annealing temperature.

Above 1800°C, we observe a decrease and a vanishing of strain in the [1 1 1] plane. TEM photographs [8] above 1600°C do not show any strain around bubbles. This agreement confirms that η can be understood as an estimation of the local strain around helium bubbles.

4.4. Cell parameters

The CDD concentration and strain, a proof of microstructural evolution of B_4C during both irradiation and isochronal annealing must act on the cell parameters, especially on the cell volume.

For each sample, cell parameters were determined. In Fig. 9, we observe a notable cell volume decrease above 60×10^{20} captures/cm^3, due to an increase of the rhombohedral angle α while the rhombohedral length a shows the opposite dependence. This is in agreement with CDD measurements which show large increase of

Table 4
Calculation of reduced temperatures χ (irradiation temperatures over temperature associated of the helium diffusion coefficient in B_4C), Strain η, CDD size a function of $N(\alpha)$ in B_4C in $\langle 1\ 1\ 1\rangle$ direction and [1 1 1] planes

$N(\alpha)$ captures/cm^3 ($\times 10^{20}$)	T (K)	χ (%)	η (10^{-3})	L/k Å	ρ
$\langle 1\ 1\ 1\rangle$ *direction*					
12	568	3.8	1.5	843	0.91
49	637	4.2	5.7	743	0.99
67	677	4.5	3.9	405	0.96
82	710	4.7	5	183	0.94
96	743	4.9	5.7	158	0.96
[1 1 1] *plane*					
12	568	3.8	1.2	1029	0.99
49	637	4.2	3.5	723	0.98
67	677	4.5	1.6	627	0.99
82	710	4.7	3.5	535	0.95
96	743	4.9	3.9	411	0.97

Legend: T is calculated using a stationary state in heat equation and thermal conductivity coefficients given by Mahagin, ρ is the linear regression coefficient of $\Delta b^2 = f(s^2)$ curves.

Table 5
CDD concentration as a function of $N(\alpha)$

$N(\alpha)$ captures/cm^3 ($\times 10^{20}$)	CDD ($\times 10^{16}$/cm^3)
12	0.11
49	0.26
67	0.63
82	1.91
96	3.74

Legend: CDD concentration is $1/(L_p^2 L_c/k_p^2/k_c)$.

CDD density above 60×10^{20} captures/cm^3 (Fig. 6). Even if the precision of CDD and cell parameters is not high, we observe a significant evolution of these parameters.

Fig. 10 shows no significant evolution the cell parameters up to 1600°C for the isochronal annealed sample, in agreement with CDD and strain determinations.

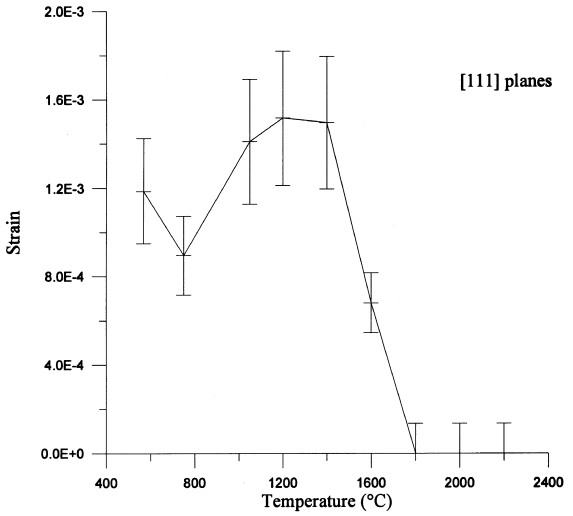

Fig. 8. Evolution of η in [1 1 1] planes as a function of annealing temperature for a annealing time of 30 min.

5. Discussion

5.1. CDD interpretation

The ordinate intercept of Δb^2 vs. s^2 curves can be understood as a characteristic length which could be due to several phenomena:

- Lithium precipitates induced by lithium production. However, such compounds have never been observed in TEM observations [2,6].
- A second phase (essentially composed of carbon) may appear during neutron irradiation. No new X-ray diffraction peaks were observed for any irradiated or annealed samples, even for high values of $N(\alpha)$.
- Helium bubbles. Bubbles concentration obtained by TEM observations is about 10^{16} cm^{-3} [2,4,6].

Fig. 6 presents also a CDD density around 10^{16} cm^{-3}. Table 6 presents a comparison between helium bubbles concentration [24] and CDD density as a func-

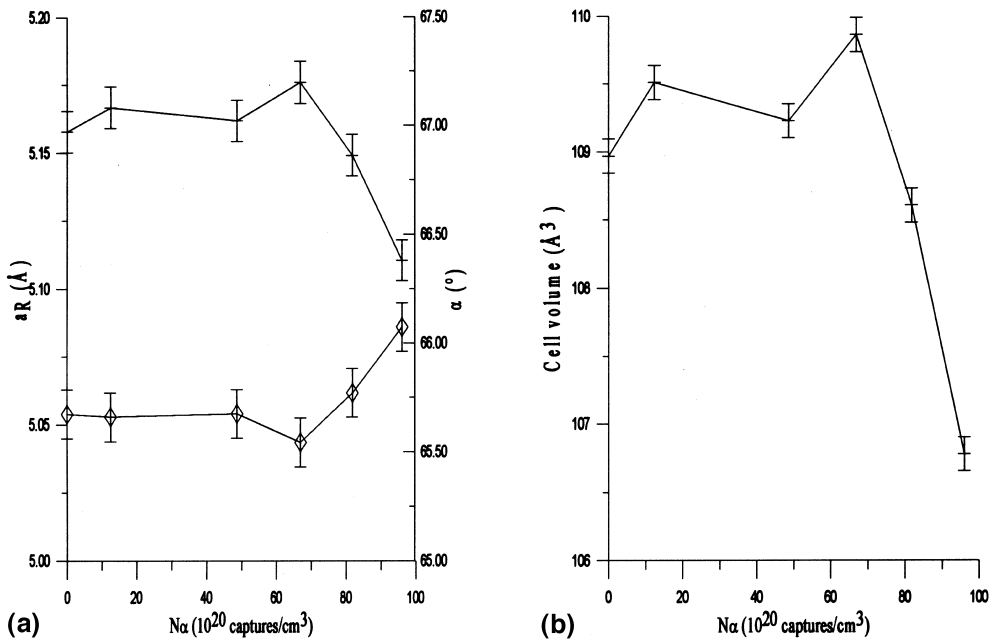

Fig. 9. Evolution of cell parameters (rhombohedral length: ×; rhombohedral angle: ◇) and cell volume as a function of $N(\alpha)$.

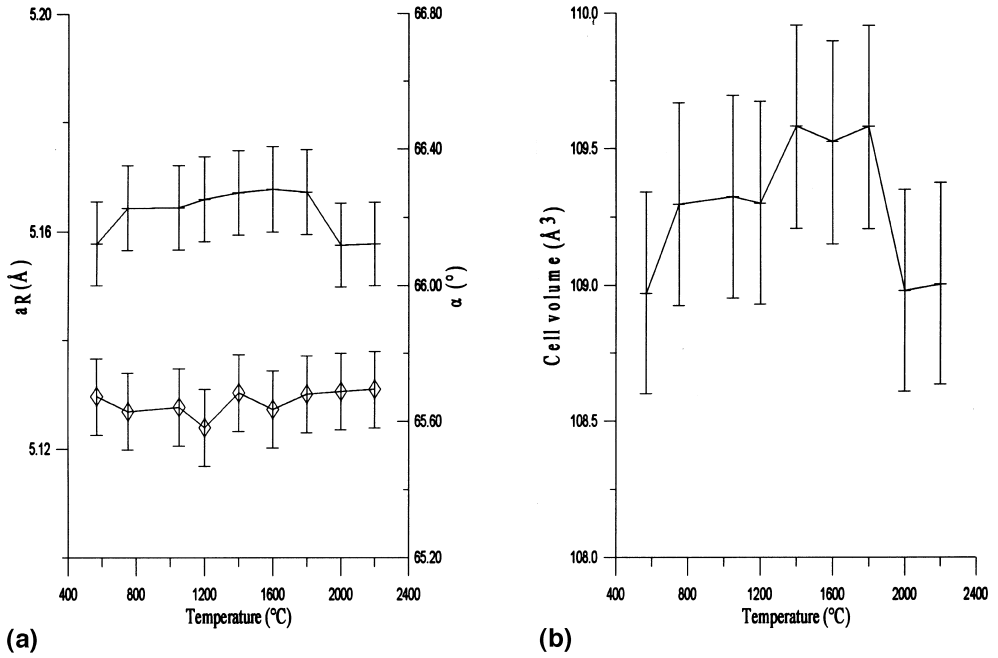

Fig. 10. Evolution of cell parameters parameters (rhombohedral length: ×; rhombohedral angle: ◇) and cell volume as a function of annealing temperature.

tion of $N(\alpha)$. We remark that CDD density is always lower than bubbles concentration. CDD density must be corrected by a factor k^3 where k is always superior to 1 in the B_4C cell. Such an effect leads to a bubbles CDD/density ratio constant as a function of $N(\alpha)$, taking into account measurement precision.

From this analysis, CDD can be understood as the domain limited by helium bubbles in the irradiated B_4C samples. The CDD is a measure of the mean length between two helium bubbles. The interest of using X-ray diffraction profile measurements is then obvious. The analysed volume by X-ray beam permits to estimate a mean bubbles density whereas TEM observations give only a local information on bubble density.

Calculated irradiation temperatures permit us to compare our results on CDD evolution with those of other authors who used the irradiation temperature to index their curves [7,8]. Because the $N(\alpha)$ value is linearly linked to the irradiation temperature in our calculations, it is not possible for us to know whether $N(\alpha)$ or irradiation temperature is the main parameter governing bubbles nucleation in irradiated B_4C samples we studied.

Table 6
Comparison of helium bubbles concentration obtained by TEM and calculated CDD concentration

$N(\alpha)$/cm^3 ($\times 10^{20}$)	χ (%)	c ($\times 10^{16}$/cm^3)	c/CDD
16	5.8	0.95	8.6
24	6.0	1.90	–
79	7.8	2.30	1.2
129	8.5	5.40	–
142	11.7	3.40	–

The mean length used in isochronal annealing to calculate the diffusion process characteristic time is equal to the measured CDD obtained on the lowest irradiated sample.

5.2. Strain interpretation

The analysis of CDD as domains limited by bubbles in the material permits to understand the strain as a maximum strain induced by bubbles in the CDD. TEM photographs show that strain (and then stress) is localized near bubbles [6]. The X-ray diffraction analysis permits to obtain a value of strain around bubbles as a function of $N(\alpha)$. There is an increase of the strain until 40×10^{20} captures/cm^3. Above this value, η remains constant. This can be understood by a bubble growth until a 'characteristic' size. Stoto's analysis of TEM observations agree with this assumption [24].

Isochronal annealing of irradiated B_4C samples gives us many informations. First, the stability of CDD strain and cell parameters below 1600°C do not show any growth of helium bubbles (no strain evolution). From this experiment, we deduce that helium atoms are rapidly trapped in bubbles during irradiation. Secondly, no

mobility of helium bubbles is observed (no CDD evolution) until 2200°C. It means that helium bubbles once they are formed are very stable. Such a stability of helium atoms can explain the low value of helium release observed [3].

5.3. Unit cell evolution

The decrease of the unit cell volume cannot be totally correlated to the strain associated to bubbles. First, because the strain induced is large only near bubbles, there is no interaction between them and only a small part of B_4C crystal is affected. Secondly, under neutron irradiation, the chemical composition of B_4C changes. There is apparition of lithium atoms which may stay diluted in the irradiated B_4C. This leads to a possible increase of angle α. Moreover, it seems that under irradiation the linear CBC chain of B_4C is destroyed [25]. This may induce a diminution of the cell parameter a. This interpretation is confirmed by our measurements (Fig. 9).

Our results on cell parameter evolution agree with results of previous works [8], but it seems difficult to link them directly to the bubble density evolution.

6. Conclusion

We have analysed X-ray diffraction lines of irradiated and annealed B_4C samples. From this analysis, we have calculated:

- a characteristic CDD size which can be interpreted as an estimation of helium bubbles concentration in irradiated B_4C;
- a value of strain η around helium bubbles.

Annealing of irradiated B_4C samples above 1800°C clearly shows a vanishing of η is agreement with expected helium bubbles relaxation previously observed on TEM photographs. In the study of η as a function of $N(\alpha)$, a saturation above 40×10^{20} captures/cm^3 appears. Such a saturation can be explained by a characteristic or limiting size of helium bubbles.

Isochronal annealing clearly shows that no second phase appears. No growth of helium bubbles is observed. After annealing near B_4C melting point (2400°C), no disappearing of helium bubbles occurs.

Form this study, we can deduce that no helium atoms stay in solid solution in B_4C. All helium atoms are trapped in bubbles, which are very stable and induce stress in the material. Helium bubbles seem to grow until a characteristic size which is not yet understood.

To confirm this work, TEM studies are in progress to obtain a more accurate analysis of helium bubbles nucleation in irradiated B_4C samples.

Moreover, it could be interesting to study with this method ^{10}B depleted B_4C samples (to avoid the self-shielding of ^{10}B) irradiated at low $N(\alpha)$ value and low temperature to obtain more accurate information on helium bubbles nucleation and then on the B_4C swelling mechanism under irradiation. For instance, B_4C pellets irradiated in PWR at 10^{20} captures/cm^3 and at 350°C may exhibit a large swelling, because we think that helium atoms may stay in solid solution in the matrix.

Appendix A. Calculation of a profile using the transparency correction

The transparency correction function can be described by h_t non-null for $0 < y < A \tan\varphi$.

$$h_t = \exp(-ay),$$
$$a = \mu\left(\frac{1}{\sin\varphi} + \frac{1}{\sin(2\theta - \varphi)}\right).$$

If we consider that g can be described by a gaussian function.

$$f(x) = \int_0^\infty \exp\left(\frac{-(x-y)^2}{s^2}\right)\exp(-ay)\,\mathrm{d}y,$$
$$f(x) = \exp\left(-\frac{x^2}{s^2}\right)\exp\left(\frac{-as^2}{4}\right)Q(x),$$

with

$$Q(x) = \int_{-(x+\frac{as^2}{2})}^\infty \exp\left(-\frac{u^2}{s^2}\right)\mathrm{d}u,$$

where $Q(x)$ is the Erf function.

For a lorentzian profile, we obtain:

$$g(x) = \int_0^\infty (b + (x-y)^2)^{-1}\exp(-ay)\,\mathrm{d}y,$$
$$g(x) = (b + (x-y)^2)^{-1}\sum_{n=0}^\infty \frac{n!}{a^{n+1}}R_n(x),$$

Where $R_n(x)$ are defined by:

$$R_n(x) = (b + x^2)\frac{\mathrm{d}^n}{\mathrm{d}y^n}\bigg|_{y=0}(b + (x-y)^2)^{-1}.$$

For instance, we have:

$$R_0(x) = 1,$$
$$R_1(x) = 2x(b + x^2),$$
$$R_2(x) = \frac{(2x^2 - 2b)}{(b + x2)^2}.$$

Then it is possible to calculate transparency correction when $g(x)$ is described by a pseudo-Voigt function.

We restrict our analysis using only gaussian functions to describe the $g(x)$ profile. Then rewriting the $Q(x)$ function, we obtain:

$$f(2\theta - 2\theta_0) = \int_0^{A\tan\varphi} \exp(-ay) \times \exp\left(-\left(\frac{2\theta - 2\theta_0 + \frac{y\sin 2\theta}{A\sin\varphi}}{\sqrt{2\Delta}}\right)^2\right)\frac{dy}{\Delta\sin\varphi\sqrt{2\pi}}$$

which can be developed in

$$f(\xi) = \exp(-2D(D-\xi)) \times \frac{\mathrm{Erf}(AB\tan\varphi + 2D + \xi) - \mathrm{Erf}(\xi)}{\mathrm{Erf}(AB\tan\varphi + 2D + \xi) - \mathrm{Erf}(D)},$$

with

$$\delta = \frac{\mu R}{\sqrt{2}\,\sin 2\theta_m}\left(1 + \frac{\sin\varphi}{\sin(2\theta_m - \varphi)}\right),$$
$$D = \delta\Delta,$$
$$\xi = D + \frac{(2\theta - 2\theta_0)}{\sqrt{2}\Delta},$$
$$B = \frac{\sin 2\theta_m}{R\sqrt{2}\Delta}.$$

For $A = 0.3$ cm, $\varphi = 10^\circ$ $\mu = 5.48$ cm^{-1}, we can simplify the function f.

$$f(\xi) = \exp(-2D(\xi - D))\frac{(1 - \mathrm{Erf}(\xi))}{(1 - \mathrm{Erf}(D))}$$

The problem consists now to calculate ξ and Δ.

Noting that f is maximum for $\xi = D$ and deriving this expression with respect to ξ, we obtain a relation between ξ and $D = \delta\Delta$.

$$D(1 - \mathrm{Erf}(\xi)) = \frac{\exp(-\xi^2)}{\sqrt{\pi}}. \quad (A.1)$$

The Erf function can be approximated by a combination of exponential and polynomes:

$$\mathrm{Erf}(x) = 1 - \exp(-x^2)P(t)$$

with

$$t = \frac{1}{1 + px},$$
$$P(t) = \sum_{i=0}^{2} a_i t^i,$$

and $p = 0.47047$.

Resolving (Eq. (A.1)) leads to solve a third order equation in t which solution is written as:

$$t^* = \mathrm{sgn}(R)\left[\sqrt[3]{E + |R|} + \frac{Q}{\sqrt[3]{E + |R|}}\right] - \frac{a_2}{3},$$

where

$$Q = \frac{a_2^2 - 3a_1}{9},$$
$$R = \frac{2a_2^3 - 9a_2 + 27a_0}{54},$$
$$E = R^2 - Q^3,$$

and

$$a_2 = -0.1282,$$
$$a_1 = 0.4653,$$
$$a_0 = -\frac{0.7544}{D}.$$

We remark that E is always positive. Then, the real solution of this equation is unique. We can now link ξ to Δ.

Δ is obtained by adjusting a three order power expansion of the calculated $f(\xi)$ curve on the experimentally collected X-ray diffraction profile.

It is then possible to build the gaussian $g(\xi)$ function from an experimental profile.

References

[1] G. Hollenberg, J. Basmajian, J. Am. Ceram. Soc. 65 (1982) 179.
[2] T. Stoto, N. Housseau, L. Zuppiroli, B. Kryger, J. Appl. Phys. 68 (1990) 3198.
[3] T. Noruyama, S. Onose, T. Kaito, M. Horiuchi, J. Nucl. Sci. Technol. 34 (1977) 1006.
[4] G. Hollenberg, B. Mastel, J. Basmajian, J. Am. Ceram. Soc. 63 (1980) 376.
[5] A. Jostsons, C. Dubose, J. Nucl. Mater. 44 (1972) 91.
[6] A. Jostsons, C. Dubose, G. Copeland, J. Stiegler, J. Nucl. Mater. 49 (1973) 136.
[7] G. Hollenberg, W. Cummings, J. Am. Ceram. Soc. 60 (1977) 520.
[8] G. Copeland, R. Donnelly, W. Martin, Nucl. Technol. 16 (1972) 226.
[9] M. Evian, P. Deniard, A. Jouanneaux, R. Brec, J. Appl. Crystallogr. 26 (1993) 563.
[10] O. Masson, R. Guinebretiere, A. Dauger, J. Appl. Crystallogr. 29 (1996) 540.
[11] O. Masson, Limoges University thesis (1998).
[12] A. Wilson, Théorie mathématique de la diffraction des poudres aux RX, Dunod, 1964.
[13] A. Klung, X-ray Diffraction Procedures, Wiley, New York, 1966.
[14] J. Berar, G. Baldinozzi, J. Appl. Crystallogr. 26 (1993) 128.
[15] A. Wilson, Proc. Phys. Soc. 80 (1962) 286.
[16] J. Langford, R. Cornik, D. Louër, J. Appl. Crystallogr. 24 (1991) 913.
[17] P. Healey, J. Ayers, Acta Crystallogr. A 52 (1996) 245.
[18] H. Longuet-Higgins, M. Roberts, Proc. R. Soc. A 230 (1955) 110.
[19] D. Mahagin, L. Bates, D. Baker, TME Report 77–33 (1977).

[20] J. Clayton, W. Bostrom, Metals Ceramics and Materials WAPD 255 (1962).
[21] H. Rietveld, Acta Crystallogr. 22 (1967) 151.
[22] H. Rietveld, J. Appl. Crystallogr. 2 (1969) 65.
[23] M. Cohen, Rev. Sci. Instr. 6 (1935) 155.
[24] T. Stoto, CEA Report, CEA-R-5389.
[25] D. Simeone, work in progress.